Ocean Modelling
September 2020, Volume 153, Pages 101673 (9p.)
https://doi.org/10.1016/j.ocemod.2020.101673
https://archimer.ifremer.fr/doc/00641/75311/

Coherent dipoles in a mixed layer with variable buoyancy: Theory compared to observations

Lahaye Noe [1], Zeitlin Vladimir [2, 3, *], Dubos Thomas [4]

[1] Univ. Brest, CNRS, IRD, Ifremer, Laboratoire d'Oceanographie Physique et Spatiale (LOPS), IUEM, Brest, France
[2] LMD, Sorbonne University and Ecole Normale Superieure, 24 rue Lhomond, 75005 Paris, France
[3] Department of Mathematics, Southern University of Science and Technology, Shenzhen, China
[4] LMD, Ecole Polytechnique, 91128 Palaiseau, France

* Corresponding author : Vladimir Zeitlin, email address : zeitlin@lmd.ens.fr

Abstract :

Motivated by recent observations of coherent dipolar cyclone-anticyclone structures in the ocean, the modons, and their signature in the surface temperature field, we demonstrate that the classical modon solutions of the barotropic quasi-geostrophic equations can be generalized to include buoyancy or temperature as an active tracer. The properties of such "thermal" modons, and especially their ability to carry heat anomaly over long distances, depend on the relative sign of the associated vorticity and buoyancy anomalies. We show using numerical simulations with the thermal shallow water equations, and their quasi-geostrophic version, that the evolution of the modons is consistent with the observations.

Highlights

► Existence of coherent dipolar vortices, the modons in a model of shallow mixed layer, with buoyancy as an active tracer, is demonstrated. ► The evolution of these structures is consistent with recent observations. ► Transport and mixing of buoyancy by the dipoles depend on relative signs of vorticity and buoyancy anomalies.

Keywords : Mixed layer, Vortex dipoles, Coherent structure

1. Introduction

Mesoscale eddies are ubiquitous features of the ocean circulation, and an important component of the ocean energetics and variability (Ferrari and Wunsch, 2009; Chelton et al., 2011). They play an active role in the transport of heat, salt, and biogeochemical constituents (Yamamoto et al., 2018; Sun et al., 2019). While isolated eddies drift westward at rather slow speed in the linear regime, especially in mid-to-high latitudes (their velocity follows the Rossby wave speed),

*Corresponding author : zeitlin@lmd.ens.fr

non-linearities can allow for anomalous propagation velocities (Chelton et al., 2011). Among nonlinear mechanisms, the pairing of counter-rotating vortices can lead to rapid propagation, which has an impact on transport properties.

Recently Hughes and Miller (2017) reported a discovery of long-living coherent dipolar structures in the ocean, and convincingly associated them with long-known modon solutions of the barotropic quasi-geostrophic (QG) equations (Larichev and Reznik, 1976). The modons detected in the data evolve on the background of inhomogeneous surface temperature, and carry with them, for some time, temperature anomalies (Hughes and Miller, 2017, Fig. 3). Modons are coherent steady-moving cyclone-anticyclone eddy pairs which capture and transport fluid masses, but both the classical (Larichev and Reznik, 1976) and more recent (Kizner et al., 2008; Ribstein et al., 2010) modon theories are essentially barotropic, and allow the inclusion of variable temperature and/or buoyancy only as passive tracers. Yet the overall temperature field in the observations does not appear to be perfectly captured by the dipoles. This suggests that temperature does not behave as a purely passive tracer, and the question of its possible influence on the evolution of the vortex dipoles arises, which is the main motivation of this work.

We recall that there exists a generalization of the classical Rotating Shallow Water (RSW) model, of which the barotropic QG model is a low Rossby number limit, allowing for inclusion of variable buoyancy as a dynamically active tracer. This is the so-called thermal shallow water (TSW) model, which was multiply reinvented in the context of the boundary layer in the atmosphere (Lavoie, 1972; Salby, 1989) and mixed layer in the ocean (McCreary et al., 1993; Young, 1994; Ripa, 1995), and share some similarities with other simplified models of the latter (*e.g.* Szoeke and Richman, 1984). The QG limit of TSW, which we will call TQG, was established by Warnerford and Dellar (2013). The typical Rossby number of the modons reported by Hughes and Miller (2017) was of the order 10^{-2} (considering the "global" Rossby number, *i.e.* $Ro = U^*/fL^*$ where U^* is the typical velocity and L^* the typical size of the modon), which makes the TQG model a good framework for investigating their dynamics. Below, we

extend the classical derivation of the modon solutions to the TQG model, and then show, with the help of numerical simulations, that such solutions exist also in the full TSW model. We demonstrate that the properties of thus obtained "thermal" modons crucially depend on the relative sign of associated vorticity and buoyancy anomalies. The evolution of the thermal modons will be shown to be consistent with the observations.

2. TSW and TQG models and existence of modon solutions

2.1. Equations of motion

The TSW model, which we will be considering in the f- plane approximation (the generalization to the beta- plane is straightforward), can be derived by vertical averaging of the primitive equations under the columnar motion hypothesis (e.g. Zeitlin, 2018, Ch. 14). The equations of the model for horizontal velocity $\boldsymbol{v}(x,y,z)$, total thickness (geopotential height) $h(x,y,z)$, and total buoyancy $b(x,y,z)$ fields read:

$$\begin{cases} \partial_t \boldsymbol{v} + \boldsymbol{v}\cdot\nabla\boldsymbol{v} + f\hat{z}\wedge\boldsymbol{v} = -b\nabla h - \dfrac{h}{2}\nabla b\,, \\ \partial_t h + \nabla\cdot(vh) = 0\,, \partial_t b + \boldsymbol{v}\cdot\nabla b = 0, \end{cases} \tag{1}$$

where $\nabla = (\partial_x, \partial_y)$. Both the thickness and buoyancy are positive, with a constant horizontally-averaged value $\overline{h}, \overline{b} > 0$. The buoyancy is related to temperature anomaly: according to the most frequent interpretation, the model describes the active upper layer of the ocean, $b = g\frac{\rho_0-\rho}{\rho_0}$, where ρ and $\rho_0 = \text{const}$ are densities of the upper and infinitely deep passive lower layers (Warnerford and Dellar, 2013). Other interpretations however exist, in the oceanic or the atmospheric context (Zeitlin, 2018) – see a discussion in Sec. 5 below. By the standard procedure, in the limit of small Rossby number, the quasi-geostrophic limit of these equations is obtained (Warnerford and Dellar, 2013, their equations 4.12 a–c):

$$\begin{cases} \partial_t\left(\nabla^2\psi - \frac{\psi-b}{Bu}\right) + \mathcal{J}(\psi,\nabla^2\psi) = 0, \\ \partial_t b + \mathcal{J}(\psi,b) = 0. \end{cases} \tag{2}$$

Here, the buoyancy b is the *anomaly* (*i.e.* $b - \overline{b}$, but we use the same symbol b, not to overcharge the notation), and the geostrophic streamfunction is $\psi = b + \eta$, where η is the thickness anomaly ($h - \overline{h}$). These equations are dimensionless: in particular x, y are non-dimensionalized by the typical length scale of the flow L^* and time t by L^*/U^*. The potential vorticity anomaly in the TQG model is $q = \nabla^2\psi - \eta/Bu$, where $Bu = R_d^2/L^{*2}$ is the Burger number and Rd is the Rossby deformation radius.

2.2. TQG modons

We now generalize the classical procedure of construction of the modon solutions (Larichev and Reznik, 1976) to the TQG case. This solution consists of a dipolar structure with a compact circular support, stationary in a frame co-moving with a constant (non-dimensional) velocity U, and is obtained by assuming a linear relation between the streamfunction and the potential vorticity. We thus look for solutions of (2) moving steadily in the zonal direction: $\psi = \psi(x - Ut, y)$, $b = b(x - Ut, y)$ whereby $\partial_t \to -U\partial_x$ in eqs. (2). Note that U will thus be the propagation speed of the modon, which can be different from typical velocities induced by the dipolar structure. In this case:

$$-U\partial_x\left(\nabla^2\psi - \psi\right) + \mathcal{J}(\psi, \nabla^2\psi - b) = 0, \tag{3a}$$

$$-U\partial_x b + \mathcal{J}(\psi, b) = 0. \tag{3b}$$

To simplify the formulas above, we here further rescaled x, y and, accordingly, U, by $\sqrt{Bu}$ and got rid of Bu. This implies that length is now measured in units of R_d instead of L.

Equation (3b) is equivalent to $\mathcal{J}(\psi + Uy, b) = 0$, whence $b = F(\psi + Uy)$, where F is an arbitrary differentiable function. Substitution of this expression in equation (3a) gives (see Appendix A)

$$\mathcal{J}\left(\psi + Uy, \nabla^2\psi - \psi - U\,y\,F'(\psi + Uy)\right) = 0, \tag{4}$$

where the prime here and below denotes an ordinary derivative of a function of a single variable. At this point we make a simplifying hypothesis by assuming

that F is a linear function with $F' = \kappa = \text{const}$. In this case the general solution of (4) obeys

$$\nabla^2\psi - \psi - U\kappa y = G(\psi + Uy), \tag{5}$$

where G is an arbitrary function. As in the classical construction (Larichev and Reznik, 1976), we consider this equation in the outer (+) and inner (−) domains separated by a circle of radius $r = a$. This parameter defines the typical scale of the flow L and is thus set by the Burger number: $a \equiv L = 1/\sqrt{Bu}$ (in units of R_d). We then suppose that G is a linear function in each of the domains: $G(\psi + Uy) = \alpha_\pm(\psi + Uy)$ with $\alpha_\pm = \text{const}$. Hence

$$\nabla^2\psi_\pm - (1 + \alpha_\pm)\psi_\pm = Uy(\alpha_\pm + \kappa_\pm). \tag{6}$$

We further consider solutions with no buoyancy anomaly in the exterior region, by setting $\kappa_+ = 0$ there.

2.2.1. External region

A decay condition is imposed in the external region: $\psi_+|_{r\to\infty} \to 0$. Hence, from (6) $U\alpha_+ = 0 \Rightarrow \alpha_+ = 0$, and

$$\nabla^2\psi_+ - \psi_+ = 0. \tag{7}$$

This equation is solved by separation of variables in polar coordinates (r, θ). By anticipating a matching with the inner solution, we choose

$$\psi_+ = A_+ K_1(r)\sin\theta, \tag{8}$$

where A_+ is a constant to be determined, and K_1 is the modified Bessel function of order 1.

2.2.2. Internal region

The solution in the internal region is sought as a combination $\psi_- = \tilde{\psi}_- + \bar{\psi}_-$, with

$$-(1 + \alpha_-)\bar{\psi}_- = Uy(\alpha_- + \kappa), \quad \nabla^2\tilde{\psi}_- - (1 + \alpha_-)\tilde{\psi}_- = 0. \tag{9}$$

(From now on we omit the subscript in κ_-). By anticipating a matching with the outer region, the solution is chosen in the form

$$\psi_- = \left(A_- J_1(\lambda r) + Ur \, \frac{\kappa - \lambda^2 - 1}{\lambda^2} \right) \sin\theta, \tag{10}$$

where A_- is a constant to be determined, J_1 is the Bessel function of order 1, and we introduced the notation $1 + \alpha_- = -\lambda^2$.

2.2.3. Matching at $r = a$

The continuity of the streamfunction across $r = a$ in the co-moving frame: $\psi_+ + Uy = \psi_- + Uy = 0$ allows to fix the constants $A_\pm$:

$$A_+ = -\frac{Ua}{K_1(a)}, \quad A_- = Ua \frac{1-\kappa}{\lambda^2 J_1(\lambda a)}. \tag{11}$$

The second matching condition at $r = a$, $\partial_r \psi_+ = \partial_r \psi_-$, leads, as usual, to a transcendental equation allowing to determine λ at a given κ:

$$\frac{J_1'(\lambda a)}{J_1(\lambda a)} = \frac{1}{\lambda a} \left(1 + \frac{\lambda^2}{1-\kappa} \right) - \frac{\lambda}{1-\kappa} \frac{K_1'(a)}{K_1(a)}. \tag{12}$$

The lowest root of this equation gives a modon solution, the higher roots give so called "shielded" modons with strongly sheared velocity field. The speed U of the modon determines its intensity, cf. (11). Note that apart from the new parameter κ the obtained solution reproduces the velocity field of the classical f-plane modon (cf. Ribstein et al., 2010). Changing the sign of κ leads to a change of the relative sign of circulation and buoyancy anomaly of a given vortex inside the modon. Thus, there exist TQG modons with inner cyclones with positive or negative buoyancy anomaly, and vice-verse for anticyclones. Below, the former will be called regular, and the latter - anomalous. An example of thickness and buoyancy anomalies of a TQG modon is presented in Fig. 1.

3. Evolution of "thermal" modons as follows from numerical simulations

3.1. Typical parameters of observed modons

We first resume the typical dynamical parameters estimated from 9 modons reported by Hughes and Miller (2017) from observations in the southern mid-

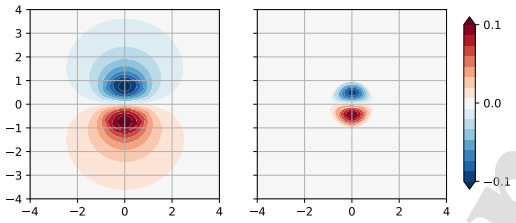

Figure 1: Thickness (*left panel*) and buoyancy anomalies (*right panel*) for a TQG modon with $\kappa = 0.5$ and $a = 1$ (regular case) in the $(x - y)$- plane in the co-moving frame. For better visualization, the buoyancy is rescaled by a factor 2.

latitude ocean (also see their Supplementary Information). For the observed dipolar structures, these dynamical parameters are in a narrow range. The typical size varies from 100 to 200 km, in an environment where the first baroclinic deformation radius is about 25 km. Although the vertical extent of the modons is not known, we can thus estimate the typical Burger number to be $0.015 - 0.07$. The mean propagation velocity of the modons is between 5 and 10 cm/s, sometimes even larger (up to 20 cm/s). The corresponding global Rossby number (U/fa), as defined in the derivation of the modon solution, is thus between 10^{-3} and 10^{-2}. As we said previously, this propagation speed does not reflect the typical velocities induced by the modon which are of order 0.5 m/s, thus corresponding to a global Rossby number approximately four times larger, while the local Rossby number number $\zeta/|f|$ is $0.1 - 0.3$. As the modons propagate in an environment with a meridional gradient of sea surface temperature (SST), the patterns of SST anomaly carried by the dipoles – which strongly depend on the location of the eddy formation – are rather diverse (Hughes and Miller, 2017, SI). Nonetheless, the temperature difference between the cyclone and the anticyclone varies typically between 0 °C, when both eddies have roughly the same SST, and 2 °C. In one single case the SST inside the cyclone is higher than in the anticyclone. This apparently narrow range of dynamical parameters may be biased by the method of observation, which is limited in resolution. Hence, the typical values of Burger number above should be considered as a

lower bound, since smaller – and potentially more ageostrophic – dipoles may exist.

In the following, we use parameters inferred from one of the modons which was tracked over a long time, and had a typical size of 100 km and a mean estimated propagation velocity of 8.8 cm/s. The temperature anomaly carried by the modon can be roughly estimated as 2°C. The corresponding buoyancy anomaly is therefore $b \approx 4 \cdot 10^{-3}$ m/s^2. Consistently with these values, we first study the evolution of a modon with an initial Burger number $Bu = 10^{-1}$, and $\kappa = \pm 0.5$ within the TQG model. Then, we extend these results to ageostrophic case using the parent TSW model.

3.2. Simulations with TQG model

To study the evolution of the modon solution derived above, we implement the TQG equations (2) with a spectral discretization in a doubly-periodic domain of size $8\,a$ and using the open-source code Dedalus (Burns et al., 2019). A Laplacian viscosity/diffusivity for the momentum and the buoyancy with a non-dimensional value of 10^{-6} is added to limit grid-scale oscillations. Time-stepping is performed using a third-order 4-step implicit/explicit Runge-Kutta scheme. We use 512 Fourier modes in each direction and a dealiasing factor of 3/2 (*e.g.* Canuto et al., 2006; Burns et al., 2019).

The evolution with positive and negative κ strongly differ. In the case of an anomalous buoyancy perturbation (negative κ), no noticeable change of shape of the modon is observed over the duration of the simulation, which was 50 in non-dimensional time units (not shown). This is an indication that such modon is a stable solution of the TQG equations (at least over time scales of a few months for typical Rossby numbers of $O(10^{-2})$). The evolution of the stream-function, potential vorticity and buoyancy of a regular modon (positive κ) is presented in Figure 2. Contrary to the anomalous modon, the regular modon rapidly develops a small-scale instability of the kind observed in Gouzien et al. (2017b). This convective-type instability leads to a complete mixing of the buoyancy field after some time. The instability generates small-scale disturbances in the

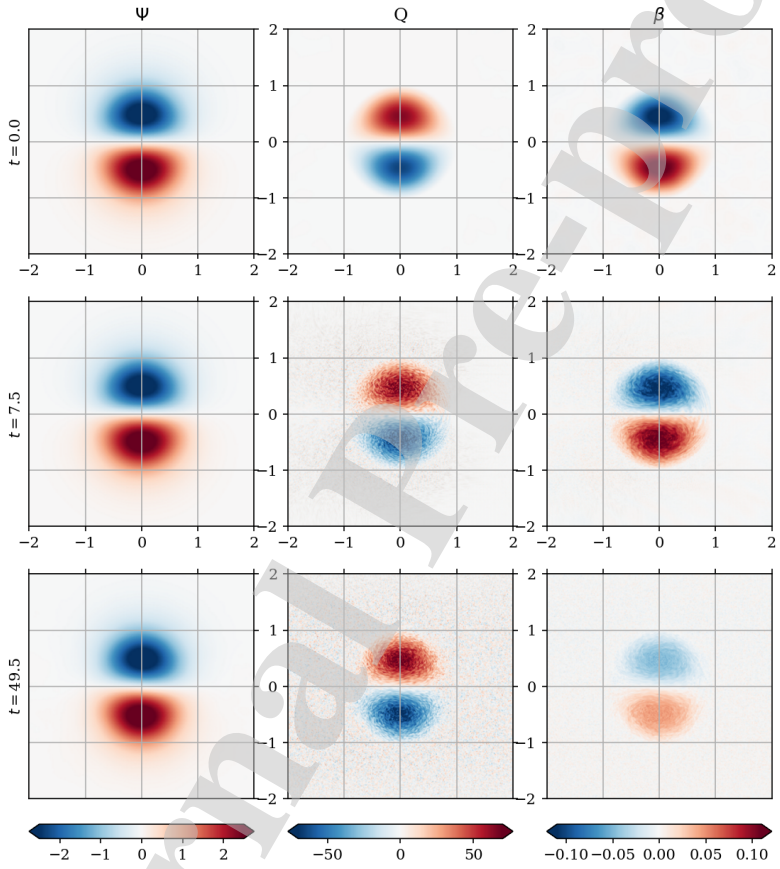

Figure 2: Evolution of the regular TQG modon: streamfunction (left column), potential vorticity (middle column) and buoyancy (right column). All quantities are non-dimensional and the domain shown is co-moving with the modon.

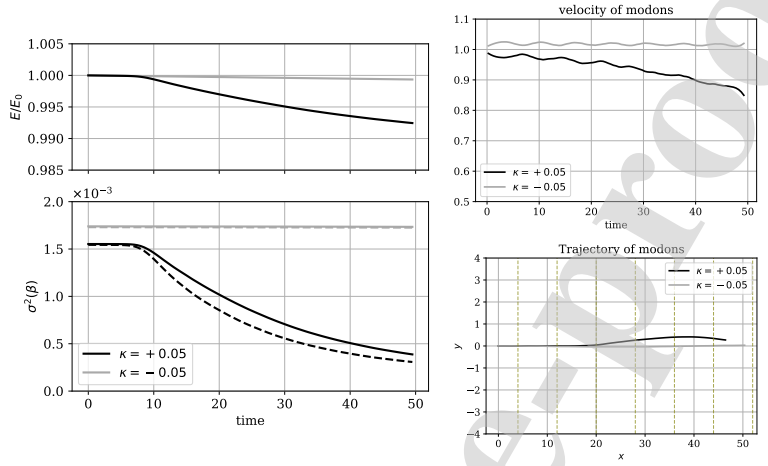

Figure 3: Evolution of the TQG energy (top left), integrated buoyancy variance (bottom left), propagation speed (top right) and trajectory (bottom right) for the unstable regular modon (black) and the stable anomalous modon (grey).

buoyancy field, as previously reported in the case of isolated vortices in the TSW model (Gouzien et al., 2017b). In the case of a planar jet, the same kind of instability in TSW model is dominated by even smaller wavenumbers than for the vortices (unpublished results, see also a discussion in the TQG case below), which is consistent with the dynamics observed in the present configuration.

Remarkably, the vorticity field keeps its coherence, leading, at the late stages of the evolution, to a steady modon with quasi-neutral buoyancy. The destruction of the buoyancy anomaly carried by the modon, and the limited modification of the modon's dynamical core are illustrated in Figure 3, where the evolution of the TQG energy (cf. Warnerford and Dellar, 2013), the buoyancy variance, and the speed of propagation of both regular and anomalous modons are shown. As seen in the figure, the instability triggers a decrease of buoyancy variance and enhances the energy dissipation, which nevertheless remains weak. The propagation velocity of the modon is also affected, exhibiting a slight decrease in course of the development of the instability. On the contrary, in the

case of the anomalous modon, all these fields (energy, buoyancy variance and propagation speed) remain practically constant during the whole simulation. This means that the decrease of energy and buoyancy variance is due to the instability, and that dissipation has a negligible impact on the evolution of the modon itself. The buoyancy variance was integrated over the whole domain (continuous line) and over the modon area only (circle of non-dimensional radius 1 – dashed lines), and divided by the area of the modon. The difference between the dashed and continuous curves is an indicator of buoyancy variance that is expunged from the modon, showing that mixing of buoyancy (and other tracers) across the edge of the dipole occurs in course of destabilization. The above results suggest that most of the buoyancy anomaly is dissipated locally, i.e. inside the modon, while a smaller – albeit not negligible – portion of it is expunged in the form of small anomalies (not captured by the color bar resolution in the corresponding snapshots in Fig. 2, right column), and then rapidly eliminated by diffusion. Because of the very small scales associated with the development of the instability, the details of the ratio of interior dissipation vs. expulsion are sensitive to the numerical resolution (the same run was repeated with 1024 Fourier modes) and the value of the diffusivity used, although the results remain qualitatively the same, and are confirmed in full TSW model below. Higher dissipation inhibits the development of the instability, resulting in a slower decrease of the buoyancy variance, and a smaller portion of buoyancy expulsion. A decrease of buoyancy mixing is observed also for the higher resolution, indicating a slow numerical convergence. Indeed, the buoyancy variance spectrum (not shown) is nearly flat at high wavenumbers down to the numerical resolution cutoff, and, probably, a more sophisticated parameterization of the horizontal mixing should be used to allow for more quantitative diagnostics. Nonetheless, this result has important implications for the transport properties of such coherent structures, which are usually characterized by their ability to isolate inner water masses from their environment and transport them over long distances. Here, the instability provides a pathway for the exchange of water between the modon and its environment, and associated reduction of the heat

anomaly.

Although detailed investigations of parameter regimes and case studies are out of the scope of the paper, we should mention that simulations of anomalous modons with $\kappa < -1$ show destabilization similar to that of regular modons.

3.3. Simulations with full TSW model

A natural question is whether the described TQG modon solutions sustain the ageostrophic corrections, in other words do ageostrophic TSW modons exist, as it is the case with "ordinary" RSW modons. Using the strategy of Ribstein et al. (2010), we initialized numerical simulations in the full TSW model (1) with the TQG modon profiles of velocity, buoyancy and thickness anomalies, as constructed above, and looked whether such initial conditions adjust to a coherent TSW structure. Following Gouzien et al. (2017b), the simulations were performed with a second-order centered finite-difference shallow-water scheme (Sadourny, 1975), which was extended to TSW by adding the corresponding terms in the momentum equations and an upwind-biased finite-volume buoyancy transport scheme. An explicit minimal Newtonian viscosity was added to the equations of the model (1) in order to regularize very small scale structures which can be produced by convective-type instabilities in TRSW, (Gouzien et al., 2017b). The values we used were $\nu \leq 10^{-3}$, with the precise value of ν having no global impact on the major features of the evolution of the modons.

Typical results from the simulations are presented in Fig. 4. The Rossby and Burger numbers of the initial TQG modons were 0.1 and 1, respectively. As in the "pure" RSW case (Ribstein et al., 2010), corresponding to $\kappa = 0$, after a period of initial adjustment, the QG modon sheds a part of cyclonic vorticity, loses its initial cyclone-anticyclone symmetry, and, as a consequence, starts moving along the curved trajectory. In the case where the cyclonic part is associated with positive anomaly of b, *i.e.* negative values of the parameter κ (anomalous modon), the dipole keeps it coherence for a long time, as in the "non-thermal" RSW case. On the contrary, in the opposite case, the regular modon undergoes a convective-type instability, as in the TQG simulations above, which

leads to a complete mixing of the buoyancy field. The instability acts more vigorously in the cyclone (as visible in the second row of Fig. 4, right panel), thus resulting in a slightly asymmetric distribution of buoyancy in the final dipole. Different stages in both cases are visualized in Fig. 4, and the "final", or "adjusted" modons in both stable and unstable cases are presented in Fig. 5.

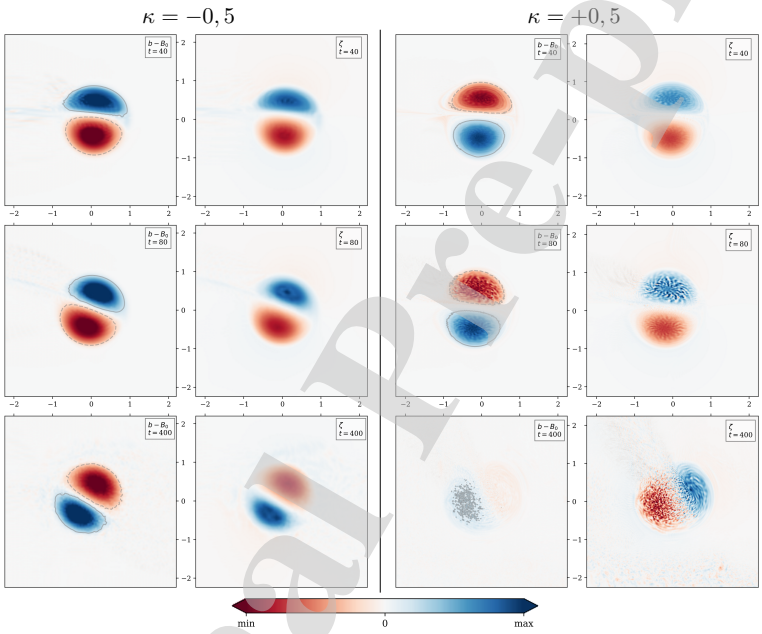

Figure 4: Snapshots of the evolution of the anomalous ($\kappa = -.5$), *left panel*, and regular ($\kappa = +.5$), *right panel*, modons. Initialization of full TSW simulations with a TQG modon with Rossby number $Ro = 0.1$ and Burger number $Bu = 1$. Min and max values in the colorbar corresponds to ± 0.05 for the buoyancy anomaly and ± 2 for the relative vorticity. Grey contour lines of buoyancy anomaly at ± 0.01 are added.

4. Jet and vortex instability in the TQG model

As discussed above, the instability observed in the modon is small scale. The difference in stability properties of the vortices depending on the sign of

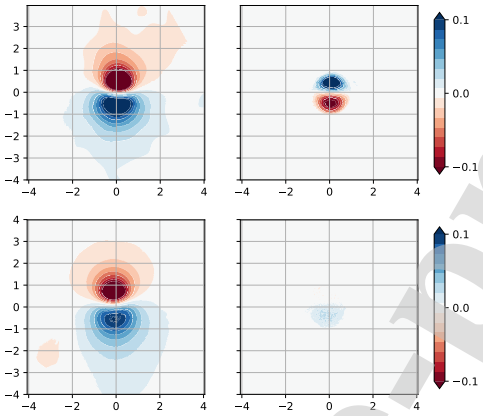

Figure 5: Adjusted stable (upper row), and unstable (lower row) modons corresponding to respective simulations of Fig. 4 at $t = 400$. *Left panels:* thickness , *right panels:* buoyancy anomaly. The latter is multiplied by 2 and fields are rotated to lie along the x-axis for better comparison with Fig. 1.

the buoyancy anomaly relative to vorticity anomaly could be anticipated in view of our previous results on the stability of monopolar vortices in the TSW model (Gouzien et al., 2017b), where we found the same dependence. Moreover, the fact that the instability is more vigorous in the cyclone – in the TSW model – agrees with the observation of Gouzien et al. (2017b) that, for the same range of parameters (Rossby and Burger numbers), the cyclones were more unstable than anticyclones.

The modons are pairs of opposite-sign vortices whose interaction gives rise to an intense jet between them, on the central axis (*e.g.* Lahaye and Zeitlin, 2012b). To get more insight on the instability of the modon in the TQG model and its implications, we investigated the evolution of jets and vortices in the TQG model in similar dynamical regimes. Initial profiles are constructed from the potential vorticity and buoyancy fields of the modon. In the case of the jet, the PV and buyancy profiles are taken from the modon solution at its center at $x = 0$, and replicated along the x-axis, and the PV equation in cartesian coordinates, which

depends on the y coordinate only, is inverted to obtain the pressure field. For the vortex, we fit the PV profile of one pole (at $y > 0$) and along the line $x = 0$ to a Gaussian bump cut from below: $Q \propto \exp(-(x/\delta))^2 - \exp(-(a/2\delta)^2), |r| < a/2$, where δ is the fitting parameter, and $Q = 0$ for $|r| > a$. Then, we invert the PV equation in polar coordinates (the corresponding equation depends on the radius r only) while imposing the buoyancy field to be proportional to this initial PV. An additional outer ring of weak negative PV anomaly is added in order to shut the far-field circulation. Dynamical parameters are the same as for the TQG modon: $Bu = 0.1, \kappa = \pm 0.5$. Additional runs with larger values of κ were also conducted to better illustrate the instability mechanism.

We first studied the linear stability of the jet. The stability diagram, which we do not present, reveals the standard barotropic instability at synoptic along-jet wave numbers (typically around $k = 2$), as expected given the alternating sign of the PV profile (*e.g.* Poulin and Flierl, 2003). In addition, for $\kappa > 0$, a small-scale instability strongly localized at the center of the jet in y-direction, and with a pronounced signature on the buoyancy field, is observed. For $\kappa < 0$, only the barotropic instability was found. In the range of investigated along-jet wavenumbers (1–19), the growth rate of the small-scale instability increases with the wavenumber, which supports the very small-scale character of the instability observed for the modons. These results are, again, in agreement with previous findings in the TSW model (Gouzien et al., 2017a).

The nonlinear evolution of this instability is investigated by means of numerical simulations in the TQG model by using the background jet with superimposed unstable mode of small amplitude as initial conditions. The results of such simulations are presented for $\kappa = 0.5$ and $\kappa = 2$ in Fig. 6, left columns. The initial stage of the instability reflects the structure of the linear unstable mode. It then exhibits a very rapid development, resulting in fast mixing of the buoyancy. While the latter remains localized near the central axis of the jet for $\kappa = 0.5$, it develops and mixes buoyancy over a much larger region for larger values of κ ($\kappa = 2$ as shown in the Figure, bottom rows, and and additional experiment with $\kappa = 5$ – not shown – further confirms this behavior).

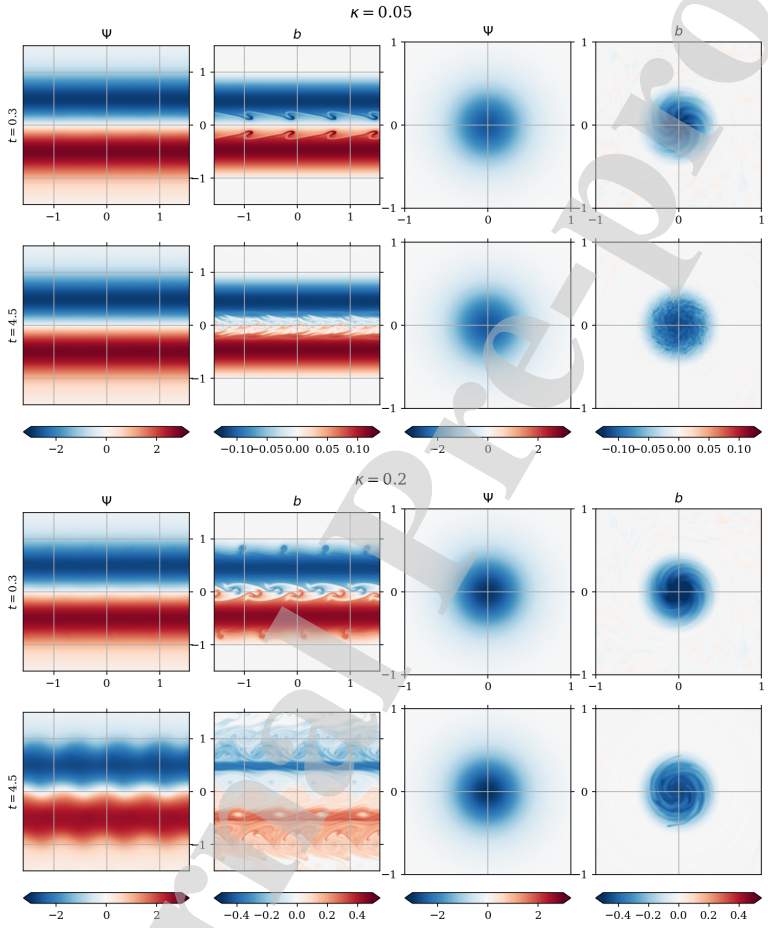

Figure 6: Instability of a jet (left pair of columns) and a vortex (right pair of columns) with $Bu = .1$ and $\kappa = +0.5$ (upper two rows) and $\kappa = 2$ (lower two rows), showing early (first and third rows) and advanced (second and last rows) stages of the instabilities as seen in the pressure (first and third columns) and buoyancy (second and last columns) fields.

The instability of vortices was investigated by superposing a weak random noise (with a relative magnitude of 2%), as well as the most linearly unstable mode found (for azimuthal wavenumber $l = 8$) with an even weaker amplitude, onto the initial buoyancy field in the initial conditions. Results from the linear stability analysis are difficult to discuss independently, because of the presence of critical layers giving rise to pseudo-modes, and would need further dedicated work. We thus rely mostly on the nonlinear simulations in the present paper, presented in Figure 6 (right columns). The vortex develops an instability very similar to the one reported by Gouzien et al. (2017b) in the TSW model, while the vortex with negative κ remains stable over the same duration (not shown). This instability is not as vigorous as in the jet configuration, and generate moderate mixing of buoyancy, which increases with the magnitude of the initial buoyancy profile.

These results thus show that the instability of the modon described in the previous section is consistent with the instabilities observed in a jet or a monopolar vortex in the TQG model. The details of the properties of the instability and its physical origin remain to be fully understood, which is left for future work.

5. Discussion

We thus demonstrated the existence of modons - coherent dipolar vortices - in a model of the mixed layer of the ocean with variable buoyancy acting as an active tracer and contributing to pressure variations. Depending on the relative orientation of circulation and buoyancy anomaly, the latter is either carried along the trajectory of the modon, or dissipated. The dissipation of buoyancy anomaly is due to small-scale convective-type instability which is not proper uniquely to the modons, but manifests itself also for jets and monopolar vortices with the same relative sign of vorticity and buoyancy anomalies. These results were obtained both in the "parent" model, namely the TSW equations, where ageostrophic effects are present and give rise to cyclone/anticyclone asymmetry

that affects the trajectory and the details of the development of the instability for the "anomalous" modon, as well as in the QG limit of this model.

We should stress at this point that the physical meaning of the results depends on the interpretation of the TSW model (and the QG limit). If it is understood as being purely barotropic, and is obtained by vertical averaging through the whole depth (Zeitlin, 2018, Ch. 14), then $b = g\frac{\rho}{\rho_0}$, where ρ and ρ_0 are the variable and constant parts of water density, respectively. This means that b decreases with temperature. If the model is understood as describing the baroclinic motions in the two-layer ocean with infinitely deep lower layer, as in Warnerford and Dellar (2013), then $b = g\frac{\rho_0 - \rho}{\rho_0}$, where ρ and $\rho_0 = \text{const}$ are densities of the upper and lower layers, i.e. b increases with temperature. As can be inferred from the observations (Hughes and Miller, 2017) the anticyclone (the observations are in the Southern hemisphere) carries for some time a positive temperature anomaly. It seems plausible (although this is not proved) that the observed dipoles are surface-intensified. In this case the second interpretation is appropriate, and observations correspond to the unstable case. However, with the realistic parameters, roughly corresponding to those in the observations, which were used in the TQG simulations, the time of mixing of the buoyancy perturbation is several months (we should recall that non-dimensional time and real time are related through the factor Ro^{-1}). This typical timescale for the elimination of the heat anomaly actually matches the observations reported in Hughes and Miller (2017, Fig. 3), where the dipole loses its temperature anomaly and exhibit entrainment of temperature anomaly from the exterior. Among other possibilities, such as interactions with an inhomogeneous environment and exterior shear/strain, the instability revealed in our simulations could be responsible for this observed behavior.

Let us finally mention that the known modon solutions in two-layer QG and RSW models, e.g. Lahaye and Zeitlin (2012a), can be generalized to the thermal counterparts of both models along the same lines as above. Yet, in order to compare such solutions with observations, an information on the deep structure is needed in these latter.

Acknowledgements

N. Lahaye was supported by a postdoctoral fellowship from CNES. The authors are grateful to the reviewers for providing useful remarks and suggestions.

Appendix A. Derivation of eq. (4)

Eq. (3a) gives, term by term and distributing the last term:

$$\mathcal{J}\left(Uy, \nabla^2\psi - \psi\right) + \mathcal{J}\left(\psi, \nabla^2\psi - \psi\right) - \mathcal{J}\left(\psi, b\right) = 0.$$

where $\mathcal{J}\left(\psi + Uy, b\right) = 0$ was used in the last term. The first two terms can be combined to give $\mathcal{J}\left(\psi + Uy, \nabla^2\psi - \psi\right)$. The last term, by virtue of $\mathcal{J}\left(\psi + Uy, b\right) = 0$, gives:

$$+\mathcal{J}\left(Uy, F(\psi + Uy)\right) = -\partial_x\psi U F'(\psi + Uy) = -\mathcal{J}\left(\psi + Uy, UyF'(\psi + Uy)\right).$$

Straightforward combination of these terms yields eq. (4).

References

Burns KJ, Vasil GM, Oishi JS, Lecoanet D, Brown BP. Dedalus: A Flexible Framework for Numerical Simulations with Spectral Methods. ArXiv190510388 Astro-Ph Physicsphysics 2019;arXiv:1905.10388.

Canuto C, Hussaini MY, Quarteroni A, Zang TA. Spectral Methods: Fundamentals in Single Domains. Springer Science & Business Media, 2006.

Chelton DB, Schlax MG, Samelson RM. Global observations of nonlinear mesoscale eddies. Prog Oceanogr 2011;91(2):167–216. doi:10.1016/j.pocean.2011.01.002.

Ferrari R, Wunsch C. Ocean Circulation Kinetic Energy: Reservoirs, Sources, and Sinks. Annu Rev Fluid Mech 2009;41(1):253–82. doi:10.1146/annurev.fluid.40.111406.102139.

Gouzien E, Lahaye N, Zeitlin V, Dubos T. Instabilities of vortices and jets in thermal rotating shallow water model. In: Topical Problems of Fluid Mechanics 2017. Institute of Thermomechanics, AS CR, v.v.i.; 2017a. p. 147–52. doi:10.14311/TPFM.2017.019.

Gouzien E, Lahaye N, Zeitlin V, Dubos T. Thermal instability in rotating shallow water with horizontal temperature/density gradients. Phys Fluids 2017b;29:101702.

Hughes C, Miller PI. Rapid water transport by long-lasting modon eddy pairs in the Southern midlatitude oceans. Geoph Res Lett 2017;44:12375–84.

Kizner Z, Reznik G, Fridman B, Khvoles R, McWilliams J. Shallow-water modons on the f - plane. J Fluid Mech 2008;603:305–29.

Lahaye N, Zeitlin V. Existence and properties of ageostrophic modons and coherent tripoles in the two-layer rotating shallow water model on the f-plane. J Fluid Mech 2012a;706:71–107.

Lahaye N, Zeitlin V. Shock Modon: A New Type of Coherent Structure in Rotating Shallow Water. Phys Rev Lett 2012b;108(4):044502. doi:10.1103/PhysRevLett.108.044502.

Larichev V, Reznik G. Two-dimensional solitary Rossby waves. Doklady USSR Acad Sci 1976;231:1077–80.

Lavoie RL. A mesoscale numerical model of lake-effect storms. J Atmos Sci 1972;29:1025–40.

McCreary J, Kundu P, Molinari R. A numerical investigation of dynamics, thermodynamics and mixed-layer processes in the indian ocean. Prog Oceanog 1993;31:181–244.

Poulin FJ, Flierl GR. The Nonlinear Evolution of Barotropically Unstable Jets. J Phys Oceanogr 2003;33:20.

Ribstein B, Gula J, Zeitlin V. (A)geostrophic adjustment of dipolar perturbations, formation of coherent structures and their properties, as follows from high-resolution numerical simulations with rotating shallow water model. Phys Fluids 2010;22:116603.

Ripa P. On improving a one-layer ocean model with thermodynamics. J Fluid Mech 1995;303:169–201.

Sadourny R. The dynamics of finite-difference models of the shallow-water equations. J Atmos Sci 1975;32:680–9.

Salby M. Deep circulations under simple classes of stratification. Tellus 1989;41A:48–65.

Sun B, Liu C, Wang F. Global meridional eddy heat transport inferred from Argo and altimetry observations. Sci Rep 2019;9(1):1345. doi:10.1038/s41598-018-38069-2.

Szoeke RAD, Richman JG. On Wind-Driven Mixed Layers with Strong Horizontal Gradients—A Theory with Application to Coastal Upwelling. J Phys Oceanogr 1984;14(2):364–77. doi:10.1175/1520-0485(1984)014<0364:OWDMLW>2.0.CO;2.

Warnerford E, Dellar P. The quasi-geostrophic theory of the thermal shallow water equations. J Fluid Mech 2013;723:374–403.

Yamamoto A, Palter JB, Dufour CO, Griffies SM, Bianchi D, Claret M, Dunne JP, Frenger I, Galbraith ED. Roles of the Ocean Mesoscale in the Horizontal Supply of Mass, Heat, Carbon, and Nutrients to the Northern Hemisphere Subtropical Gyres. J Geophys Res Oceans 2018;123(10):7016–36. doi:10.1029/2018JC013969.

Young W. The subinertial mixed layer approximation. J Phys Oceanogr 1994;24:1812–26.

Zeitlin V. Geophysical Fluid Dynamics. Oxford University Press, 2018.

Noe Lahaye: Conceptualization, Methodology, Software, Visualization, Writing.
Vladimir Zeitlin: Conceptualization, Methodology, Writing, Formal Analysis, Writing.
Thomas Dubos: Methodology, Software

None of the authors has to declare any conflict of interest regarding the content of this manuscript